Applied organic-inorganic nanocomposite of PLA-TiO_2 for preparing polysulfone membrane: structure, performance and UV-assisted cleaning strategy

Siru Zhou, Yang Zhang, Lei Ni, Yuxiang Pei, Haoquan Zhang and Hongwei Zhang

ABSTRACT

Blended organic copolymer (or homopolymer) and inorganic nanoparticles have been widely used (separately or simultaneously) for optimizing membrane pore structure and surface functionality. However, the prepared membranes suffer from degraded stability and insufficient integrity due to the high solubility or incompatibility of the blending additives. In this work, an organic-inorganic nanocomposite (i.e., PLA-TiO_2) was designed, and employed for PSF membrane preparation. The Fourier transform infrared spectroscopy (FTIR) and X-ray photoelectron spectroscopy (XPS) analysis confirmed that bidentate chelating dominated the bonding mechanism between PLA and TiO_2. The resultant PSF/PLA-TiO_2 membranes possessed a highly porous surface with narrowed pore size distribution, demonstrating the strong pore forming ability of PLA-TiO_2 for membrane preparations. Moreover, owing to the distinct inorganic-organic molecular conformation, the PLA-TiO_2 exhibited enhanced stability and dispersibility within the PSF substance, which endowed the membrane with long-acting hydrophilicity and UV responsiveness. Given the UV responsiveness that is introduced by PLA-TiO_2, UV-assisted strategies (UV-F and UV-C) were designed to further mitigate membrane fouling. The fouling analysis indicated that both reversible fouling and irreversible fouling were reduced in the UV-C process, signifying the synergistic effect between photocatalysis and hydraulics in membrane fouling mitigation. The enhanced membrane performance and the efficient preparation process highlight the potential of PLA-TiO_2 in membrane modifications.

Key words | antifouling performance, PLA-TiO_2 nanocomposite, UF membrane, UV-assisted cleaning

Siru Zhou
Hongwei Zhang
School of Environmental Science and Engineering,
Tianjin University,
Tianjin, 300350,
China

Yang Zhang (corresponding author)
Lei Ni
Yuxiang Pei
Haoquan Zhang
School of Environmental Science and Engineering,
State Key Laboratory of Separation Membranes and Membrane Processes,
Tiangong University,
Tianjin 300387,
China
E-mail: *yangzhang@tiangong.edu.cn*

HIGHLIGHTS

- An organic-inorganic nanocomposite (PLA-TiO_2) was designed for membrane fabrication.
- PLA-TiO_2 exhibits strong ability for tailoring pore structure.
- Organic-inorganic conformation endows PLA-TiO_2 with enhanced stability in polymer matrix.
- UV-assisted physical cleaning significantly reduced membrane fouling resistance.

doi: 10.2166/wst.2020.564

GRAPHICAL ABSTRACT

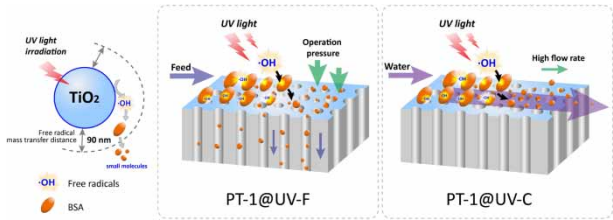

INTRODUCTION

Ultrafiltration (UF) technology has been widely accepted as an effective approach for water and wastewater treatment due to its outstanding sieving ability, compact design and sufficient stability (Khan *et al.* 2018). However, the polymeric UF membrane still suffer economic and technical challenges when applied in applications, including the trade-off between membrane selectivity (pore size) and permeability (porosity), and the severe membrane fouling resulting from low surface energy (Xing *et al.* 2019). For instance, large pores on a membrane surface are preferable to achieve better permeability, but sacrifice selectivity; different pore structures result in distinct fouling behavior with various water sources; a hydrophilic membrane surface can serve as a strong fouling barrier, etc. Therefore, in order to prepare an ideal membrane with proper pore structure and surface physicochemical properties, various strategies have been investigated to improve membrane performance during the manufacturing process, including coating, blending, and surface grafting.

Among those, the blending modification was found to be one of the most powerful ways to optimize the membrane structure and surface property simultaneously, thus extensive works have been conducted with various modifiers (Jhaveri & Murthy 2016). On the one hand, hydrophilic polymers, in particular polyvinylpyrrolidone (PVP) and polyethylene glycol (PEG) derivatives, have been widely used for improving membrane surface porosity and hydrophilicity due to their low cost and accessibility (Han & Nam 2002; Liu *et al.* 2003). Nevertheless, these water-soluble polymers have a strong tendency to leach out from the polymer matrix, resulted in decreased selectivity and hydrophilicity (Zhao *et al.* 2011). In contrast, amphipathic copolymers have recently received much attention in membrane modifications. Distinct from conventional hydrophilic additives, the hydrophilic groups within the amphipathic copolymers tend to segregate to the membrane surface and pore walls, while the hydrophobic blocks can anchor in the polymer matrix due to the hydrophobicity, eventually exhibiting enhanced compatibility (Loh & Wang 2013). Nonetheless, cost and industrial feasibility are still two key problems that baffle the large-scale application of amphipathic copolymers.

On the other hand, functional inorganic nanoparticles were also deemed as good candidates for membrane modifications (Rabiee *et al.* 2014). For instance, blending TiO_2 nanoparticles, a conventional photocatalyst, can not only manipulate the surface hydrophilicity and pore structure of a UF membrane, but can also endow the membrane with photocatalytic functionality, eventually enhancing membrane antifouling performance and self-cleaning ability under ultraviolet (UV) light (Xu *et al.* 2016). Unfortunately, previous literatures have demonstrated that using unmodified inorganic nanomaterials as an additive led to unavoidable pore structure defects and undesired performance owing to their aggregation and poor compatibility with organic substances (Shi *et al.* 2019). Accordingly, the leaching of inorganic particles during the filtration process would result in degraded membrane performance, which is a potential threat for membrane performance and effluent quality. Thus, in order to improve both the antifouling performance and pore structure of a membrane, finding a cost-effective and powerful modifier is still highly desirable.

Inspired by the above analysis, hydrophobic polylactic acid (PLA), a biodegradable, and eco-friendly polymer has attracted our attention. According to the thermodynamic mechanisms of the non-solvent induced phase separation process (NIPS), blending a foreign polymer can increase the thermodynamic instability of a membrane casting system, which favors instantaneous de-mixing and finally results in a porous structure (Li *et al.* 2016). Thus, there are reasons to infer that PLA can act as a pore forming agent for preparing porous

organic membranes. More importantly, it is reported that TiO_2 was an effective modifier for PLA in previous literatures. Xiong *et al.* (2017) coated TiO_2 on a PLA membrane, and the firmly inlaid TiO_2 enabled an efficient membrane oil/water separation property. Zhou *et al.* (2019) successfully coated TiO_2 on PLA film by the sol–gel method and the resultant membrane exhibited high permeation flux and ideal filtration efficiency. Feng *et al.* (2019) found that the PLA matrix acted as a good stabilizing agent for the TiO_2 in PLA/TiO_2 composites, and the addition of TiO_2 facilitated the mechanical and antibacterial activity of PLA film. Thus, there are reasons to expect that PLA can act as an organic template to bond with inorganic particles, then facilitate the preparation and functionalization of porous UF membrane.

In this work, an organic-inorganic nanocomposite, PLA-TiO_2, was synthesized and employed for the modification of porous PSF membrane. The binding chemistry of the prepared nanocomposite was investigated by Fourier transform infrared spectroscopy (FTIR) and X-ray photoelectron spectroscopy (XPS), and its effect on membrane morphology was analyzed from the aspect of thermodynamics and kinetics according to the SEM images. Moreover, the chemical composition, surface wettability and thermal properties of the resultant PSF/PLA-TiO_2 (PT) membranes were systematically analyzed by FTIR, XPS, water contact angle and TG methods, respectively. Besides, the antifouling performance and the self-cleaning ability of the resultant membrane under various conditions were also checked and compared with the unfunctionalized PSF membrane, suggesting the feasibility and advantages of the PLA-TiO_2 nanocomposite in membrane modifications.

MATERIALS AND EXPERIMENTS

Materials

The PSF was purchased from Shanghai Shuguang Chemical Plant (Shanghai, China). A commercial polylactic acid (PLA, molecular weight = 100,000 kDa) was obtained from NatureWorks LLC, USA. TiO_2 P25 nanoparticles were obtained from Degussa Co., Germany with an average primary particle size of approximately 21 nm (about 85% anatase and 15% rutile). The analytical grade dimethylacetamide (DMAc), NaClO were purchased from Benchmark Chemical (Tianjin, China). Reagent grade bovine serum albumin (BSA) were purchased from the Sigma-Aldrich Co., Ltd (St Louis, MO, USA). All solutions were prepared using Milli-Q™ water.

Preparation of PLA-TiO_2/PSF membranes

PLA-TiO_2 nanocomposite were fabricated by sol-gel method. Initially, TiO_2 powders and PLA pellets were dried at 65 °C and 50 °C for 24 h, respectively. Secondly, a certain amount of PLA pellets was dissolved in DMAc solution at 10 wt.%, and the temperature was set at 100 °C. Then, 2 wt.%, 5 wt.% and 10 wt.% TiO_2 (with respect to PLA) was added to the above solution respectively, and the mixtures were ultrasonically treated for an hour. The resulting mixture was vigorously stirred for another 12 h with the temperature of 80 °C. The reaction product was then separated by centrifugation at 12,000 rpm for 30 min. Subsequently, the precipitates were re-dispersed in methanol and DI water, and the above centrifugal separation process was repeated for 6–7 times to completely remove unreacted TiO_2 (Jafarpour *et al.* 2014). Finally, PLA-TiO_2 nanocomposite were obtained after drying for 4 h at 80 °C.

Membranes were prepared by using the NIPS method. The casting solution was prepared in a 250 mL conical flask by mixing polymer (PSF), nonsolvent additive and solvent (DMAc) in sequence. All casting solutions were stirred with a stir bar at 400 rpm using a digital stirring hot plate (Corning, MA). After, polymers were dissolved and stirred for at least 24 hours, the resulting solution was degassed for at least 12 hours until no visible gas bubbles were present. The solution was cast on a first-grade surface optical mirror using an 8-inch–wide doctor blade (Universal blade applicator, Paul N. Gardner Company, Inc.; Pompano Beach, FL). Then, the mirror was left in the DI water coagulation bath for 0.5 hours until the membrane detached from the mirror. Prior to further experiments, all membranes were soaked in DI water for 24 hours. The compositions of casting solution are listed in Table 1.

Characterization methods

A Nicolet iS50 spectrometer (Thermo Scientific, USA) was used to investigate the bonding chemistry of PLA-TiO_2. All spectrums were recorded over the range of 400–4,000 cm^{-1}. A K-Alpha XPS (Thermo-Fisher Scientific, FL, USA) was used and the XPS spectra were obtained by sweeping over electron binding energies of 0–1,350 eV with a resolution of 1 eV. The UV–Vis diffuse reflectance spectra (DRS) of samples were obtained using a Shimadzu 1800 spectrometer in the range of 200–700 nm. The Raman spectra were collected on a Renishaw inVia Reflex micro-Raman spectrometer with 532 nm laser excitation.

Table 1 | Compositions of casting solutions of PSF membranes

Code	Casting solution[a]	Bath	Additive	Concentration (wt%)
P0	PSF/DMAc = 14/86	DI water	NA	NA
PT-0.5	PSF/PLA-TiO_2/DMAc = 14/0.5/85.5	DI water	PLA-TiO_2	0.5%
PT-1	PSF/PLA-TiO_2/DMAc = 14/1/85	DI water	PLA-TiO_2	1%
PT-3	PSF/PLA-TiO_2/DMAc = 14/3/83	DI water	PLA-TiO_2	3%
PP-0.5	PSF/PLA/ DMAc = 14/0.5/85.5	DI water	PLA	0.5%
PPT-1	PSF/PLA[b]/ TiO_2/DMAc = 14/1/85.5	DI water	PLA + TiO_2	1%
T-1	PSF/ TiO_2/DMAc = 14/1/85	DI water	TiO_2	1%

[a]The composition of casting solutions is calculated basing on wt.%.
[b]The PLA and TiO_2 were added to the solution separately.

The membrane surface morphology was observed by Gemini SEM500 scanning electron microscope (ZEISS Group, Oberkochen, Germany) at a voltage of 10.0 kV. Image Pro Plus V.7.0 software (Vashaw Scientific, Inc., Roswell, GA, USA) was used for image statistical analysis. Since the SEM device was equipped with an energy dispersive X-ray analysis (EDAX) detector, Ti element mapping was conducted to observe the distribution of PLA-TiO_2 in the membrane matrix.

The species of active radicals were detected by electron spin resonance (ESR) technique using DMPO as spin-trapping agent. The membrane tensile strength was measured by using an electronic universal testing machine (Mecmesin, United Kingdom). The initial gauge length was 15 mm, and the testing speed was set at 200 mm/min. The membrane thermal stability was investigated using a thermal gravimetric analyzer (STA449F3, Netzsch, Germany), and the measurements were performed in a nitrogen atmosphere with a heating rate of 10 °C/min. The water contact angle on each membrane surface was measured by a DSA-25S micro-drop shape analyzer (KRŰSS GmbH, Hamburg, Germany), and the instantaneous image of the water drop on the sample surface of five random locations was recorded to calculate the water contact angle. All measurements were taken at least in triplicate with separate samples.

Filtration experiments

All membrane filtration experiments were performed using a cross-flow ultrafiltration device at 25 °C. Permeate was collected and weighed using a ME2002T balance (Mettler-Toledo, LLC, Columbus, OH, USA), and the velocity of the retentate was calculated by a flow meter to indicate the cross-flow rate. Before the experiment, the membranes were pressurized at 0.1 MPa with DI water for at least 30 min until a stable flux was reached, then the membrane initial flux was recorded as J_{w0}.

The membrane porosity is the ratio of pore volume to the membrane volume, and can be derived by the mass loss of wet membrane after drying (Luo *et al.* 2018):

$$\varepsilon = \frac{(m_w - m_d)/\rho_w}{(m_w - m_d)/\rho_w + m_d/\rho_p} \times 100\% \quad (1)$$

where m_w and m_d is the mass of wet membrane sample and dry membrane sample respectively. ρ_w is the water density and ρ_p is the PSF density (1.24 g/cm^3).

In sieving experiments, the concentration of BSA feed solution was 100 mg/L. The concentration of feed (C_f) and permeate (C_p) solutions were determined by UV–vis spectrophotometer at a wavelength of 280 nm. The rejection percentage can be expressed as:

$$R(\%) = \left(1 - \frac{C_p}{C_f}\right)100 \quad (2)$$

The fouling experiments were performed using a solution of BSA (80 mg/L) as model foulant. In order to test the antifouling performance of the composite membranes under different conditions, a UV lamp was coupled with the cross-flow filtration device to irradiate the membrane surface. The peak wavelength of the UV lamp was 254 nm, and the light intensity at the membrane surface was 13 W/cm^2. For each membrane, the flux decline was measured with a trans-membrane pressure (TMP) of 0.1 MPa, where the cross-flow rate was about 1 m/s and the flux was recorded as J_p. Each fouling test ran for 60 min, then physical cleaning was performed with deionized water for 5 min, in which the cross-flow rate was

controlled at 2 m/s by adjusting the valves. Moreover, the effect of UV irradiation on fouling stage and physical cleaning stage was also evaluated by parallel experiments. For each condition, the recovered flux was recorded as J_{w1}. Afterwards, the flux recovery ratio (FRR) was estimated as follows:

$$FRR(\%) = \frac{J_{w1}}{J_{w0}} \times 100 \quad (3)$$

Fouling of membranes can be ascribed to the formation of a cake/gel layer on the membrane surface and/or adsorption onto the membrane surface or within the membrane pores. To further analyze this process, the fouling resistance parameters of membranes were described by the following equations, including total fouling ratios (R_t), reversible fouling ratio (R_r) and irreversible fouling ratio (R_{ir}) of the membrane, respectively:

$$R_t(\%) = \frac{J_{w0} - J_P}{J_{w0}} \times 100 \quad (4)$$

$$R_r(\%) = \frac{J_{w1} - J_P}{J_{w0}} \times 100 \quad (5)$$

$$R_{ir}(\%) = \frac{J_{w0} - J_{w1}}{J_{w0}} \times 100 \quad (6)$$

$$R_t = R_r + R_{ir} \quad (7)$$

RESULTS AND DISCUSSION

Characterization of PLA-TiO_2 nanocomposite

In this study, to explore the potential ability of organic-inorganic nanocomposite as both membrane pore forming agent and antifouling modifier, the PLA-TiO_2 nanocomposite was intentionally prepared by using the sol-gel method. Figure 1(a) shows the FTIR spectra of neat PLA pellets and PLA nanocomposites synthesized with different TiO_2 loadings (2, 5 and 10% were mass fractions of TiO_2 with respect to PLA pellet).

For neat PLA pellets, two typical peaks at 1,748 cm^{-1} and 2,944 cm^{-1} could be observed, which corresponded to the stretching vibration of carbonyl (C = O) and -CH_3 group (Li *et al.* 2017), respectively. In contrast, for each PLA-TiO_2, two new peaks emerged at 1,550 and 1,457 cm^{-1}, indicating the formation of antisymmetric ($\nu(COO)_{asym}$) and symmetric ($\nu(COO)_{sym}$) coordinated carboxylate ligands with TiO_2, respectively (Green *et al.* 2012). Moreover, the normalized ratio of $\nu(COO)_{asym}$ (assigned to PLA-TiO_2) to C = O bonds (assigned to PLA) increased with TiO_2 dosing until 5 wt.% of TiO_2 was added to the solutions (see Figure S1, Supplementary Information), suggesting that in such a situation the active sites within PLAs have sufficiently reacted with TiO_2. On the other hand, the distance between antisymmetric and symmetric ligands ($\Delta = \nu_{asym}$-ν_{sym}) can be utilized to characterize their

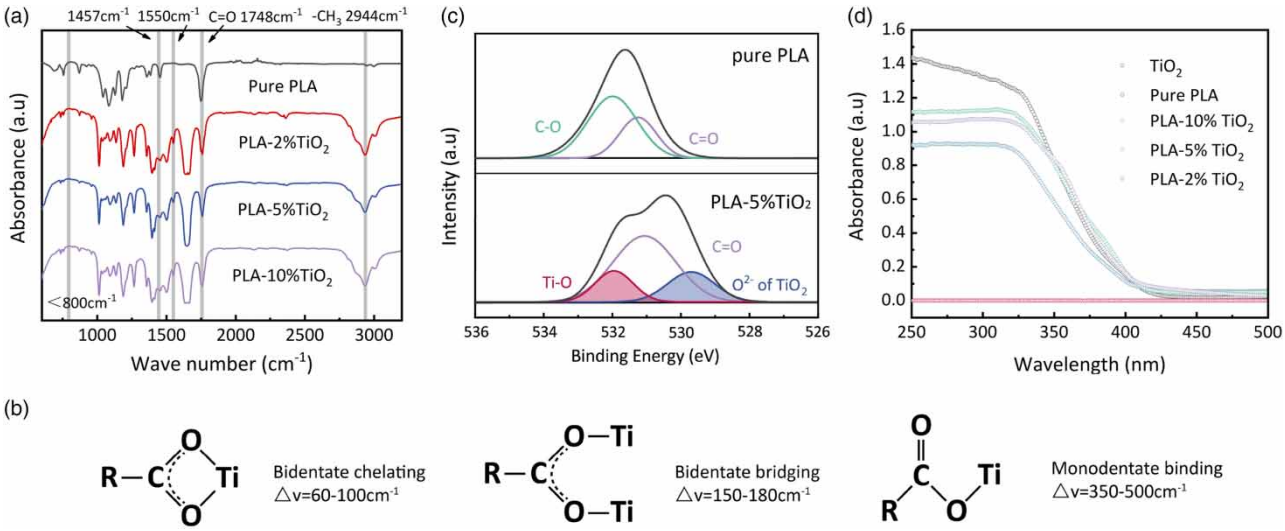

Figure 1 | (a) FTIR spectra of neat PLA and PLA-TiO_2 nanocomposite; (b) binding mode of bidentate chelating, bidentate bridging and monodentate binding; (c) O1s spectra of neat PLA and PLA-5%TiO_2; (d) UV–Vis spectra of TiO_2, neat PLA and PLA-TiO_2.

binding forms (Lee *et al.* 2000). As Figure 1(b) shows, the distance (Δ) in the range of $350-500\ cm^{-1}$, $150-180\ cm^{-1}$ and $60-100\ cm^{-1}$ represents the formation of monodentate binding, bidentate bridging and bidentate chelating (Qu *et al.* 2010), respectively. In this study, the Δ value of each nanocomposite was $\sim 93\ cm^{-1}$, indicating bidentate chelating dominated the bonding mechanism of PLA-TiO_2. Also, it was noticed that there was a broad and intensified absorption below $800\ cm^{-1}$ for each nanocomposite, which further proved the presence of covalent bonds between PLA and TiO_2 (You *et al.* 2012).

XPS was employed to further investigate the binding energy of PLA-TiO_2, and the O1s spectra of neat PLA and PLA-5%TiO_2 are shown in Figure 1(c). For PLA-5%TiO_2, the new peaks that emerged at 529.7 and 531.9 eV could be assigned to the O^{2-} anions of the TiO_2 and bidentate chelating of the Ti-O bonds (Liu *et al.* 2017), respectively. It confirmed the reaction between TiO_2 and PLA. The peak at 531.2 eV corresponding to the C = O group of PLA is shifted to the lower binding energy side, suggesting that the chemical environment around O is different from that of neat PLA. Furthermore, Figure 1(d) compares the UV–vis spectra of PLA-TiO_2 with neat TiO_2 and PLA. Clearly, neat PLA did not show any UV absorption, while the prepared PLA-TiO_2 nanocomposites exhibited strong optical responsiveness within the UV band. The UV absorption ability of the nanocomposite was increased with TiO_2 loadings, which is in line with the spectra of TiO_2 particles, also suggesting TiO_2 endowed the nanocomposite with an imaginable photocatalytic functionality.

Characterization of the PLA-TiO_2 blended PSF membranes

Membrane morphology and pore size

Figure 2 shows the top surfaces, cross-sectional morphologies and pore size distributions of PLA and PLA-TiO_2 blended PSF membranes. Compared with pure PSF membrane (see Figure S2), the surface of PP-0.5 becomes highly porous with the addition of merely 0.5 wt.% PLA. However, there are some large pores that were randomly distributed on the membrane surface, which resulted in a relatively wide pore size distribution. Also, blending of PLA significantly promoted the formation of macrovoids in the membrane sub-layer, suggesting the strong pore forming ability of PLA for PSF membranes. As for the T-1 membrane (see Figure S2), a dense top surface with randomly distributed pores was observed, and its sub-lay turned to a typically finger-like structure, implying adding TiO_2 significantly changed the kinetics and thermodynamics of the membrane formation process.

Instead, it can be seen that if 0.5 wt.% of PLA-TiO_2 were added to the casting solution, both surface and sub-layer of the resultant PSF membrane (i.e. PT-0.5) were less porous than that prepared with PLA alone (i.e. PP-0.5). Although the pore density of PT-0.5 was lower than that of PP-0.5 (see Table 2), the well-constructed pores endow the membrane with a relative narrow size distribution where over 80% of the pores were in the range of 5–20 nm. Moreover, the macrovoids were successfully suppressed on the cross-section of the PT-0.5, in which the narrow finger-like morphology is favorable for membrane mechanical properties. On the other hand, the surface porosity can be further enhanced when the loading of PLA-TiO_2 increased to 1 wt.% or more for PT-1 and PT-3 membrane (Table 2), and the membranes' cross-sectional structure was still maintained in finger-like morphology without macrovoids. In particular, the PT membrane surfaces possessed very concentrated size distributions (Figure 2, shown in the far-right columns), which possibly favored the demand on membrane selectivity.

The above observation is highly related to the thermodynamics and kinetics of the membrane formation process. For the PLA additive (PP-0.1 membrane), the highly porous structure indicated that the nucleation of the polymer-lean phase of PSF/DMAc/PLA system was significantly enhanced compared to the PSF/DMAc system (Wang *et al.* 2011). On the one hand, the strong hydrophobic-hydrophobic interactions between PSF and PLA were expected due to their hydrophobic nature, in which the polymer entanglement would disrupt the rearrangement of PSF chains in the phase inversion process, thus prolonging the solidification time of the membrane (Li *et al.* 2016). In this situation, the polymer-lean phase has sufficient time to grow into large pores. On the other hand, the enhancement of the polymer-lean phase could further accelerate the diffusion between solvent and non-solvent, placing the casting system into a thermodynamic metastable condition (Loh & Wang 2013). As a consequence, the intensified instantaneous demixing would promote the formation of macrovoids in the membrane sublayer.

For PLA-TiO_2, the porous surfaces with their fine pore structure demonstrated the unique effect of an organic-inorganic composite (i.e. PLA-TiO_2) on the membrane formation mechanisms. Compared with pure PSF membrane, the enhanced pore density of the PT membranes indicated that adding PLA-TiO_2 decreased the thermodynamic stability of the casting system, which promoted the

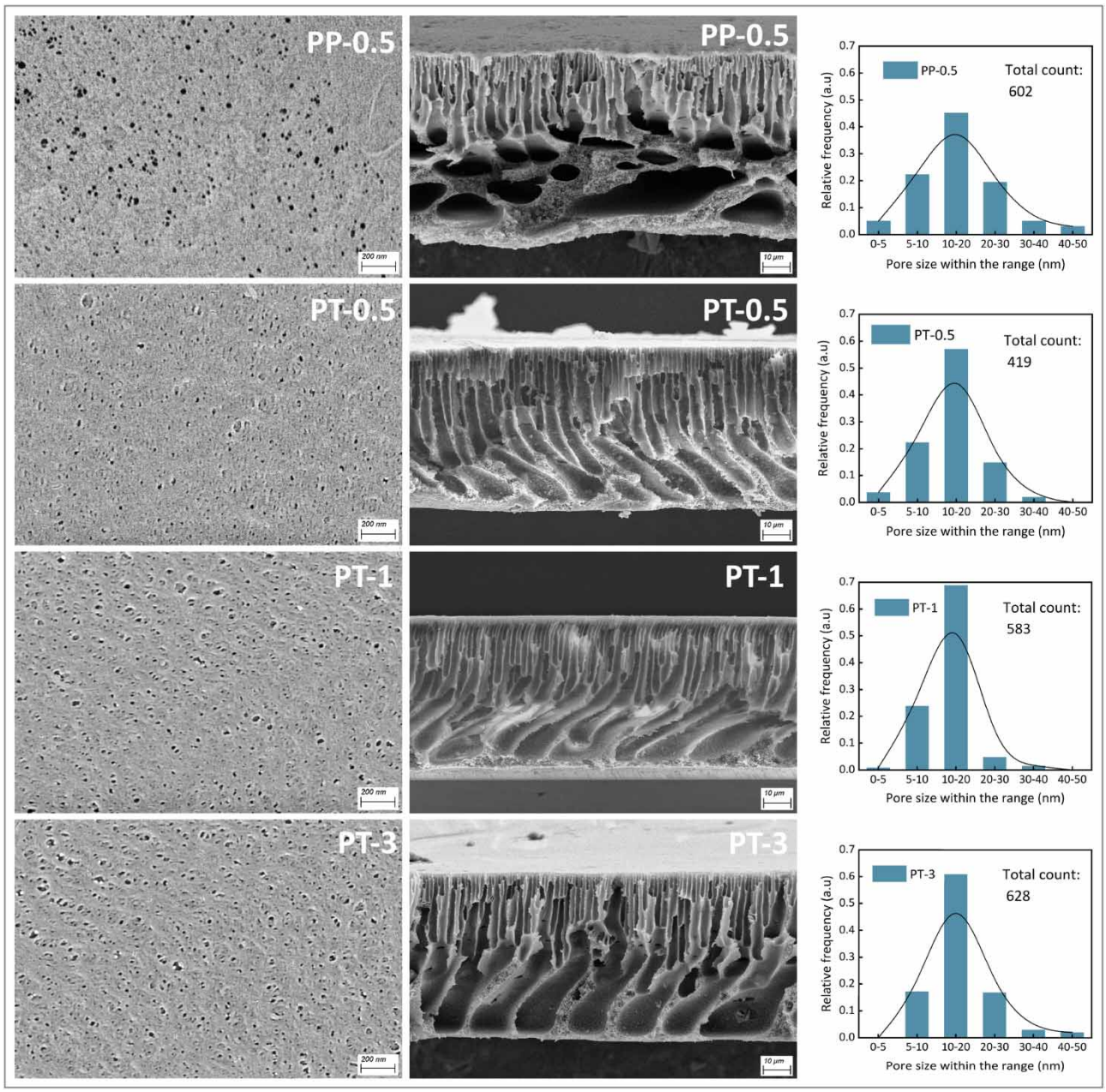

Figure 2 | Surface, cross-section images and pore size distributions of the PSF/PLA membrane (PP membrane) and PSF/PLA-TiO_2 membranes (PT membrane).

Table 2 | Properties of the prepared membranes

Membrane	Membrane porosity (%)	Pore density[a] (m^{-2})	Average surface pore size (nm)
P0	63.2 (± 1.9)	–	–
PP-0.5	81.9 (± 2.4)	1.89×10^{14} (±0.1)	13.4 (± 1.5)
PT-0.5	75.8 (± 2.1)	1.30×10^{14} (±0.02)	12.6 (± 1.1)
PT-1	80.7 (± 1.5)	1.81×10^{14} (±0.04)	14.1 (± 0.6)
PT-3	83.3 (± 2.2)	1.95×10^{14} (±0.05)	15.1 (± 1.3)

[a]Pore density was calculated from the number of pores on membrane surface.

nucleation of polymer-lean phase and formation of pores. However, different from the PP membrane and the organic PLA additives, the regulated pore diameter of PT membranes could be attributed to the strong interactions between inorganic TiO_2 and DMAc, decreasing the dissolving capacity of the solvent for PSF (Loh & Wang 2013). As a result, the rapid solidification of the surrounding polymer-rich phase could limit the growth of the polymer-lean phase (i.e. nuclei), and finally reduced pore diameters.

Moreover, for PLA-TiO_2, the solvent-nonsolvent exchange rate is expected to be reduced since previous studies have demonstrated that the presence of inorganic particles can dramatically increase the viscosity of dope solutions (Méricq *et al.* 2015). As a result, slow in-diffusion of non-solvent tended to delay the phase inversion process, where the liquid-solid (L-S) demixing was promoted, and the macrovoid growth was therefore suppressed. Such inference could also be proved by the SEM image of the T-1 membrane (Figure S2): adding TiO_2 endows the membrane with a dense top surface and narrowed finger-like sub-layer.

Furthermore, when the concentration of PLA-TiO_2 increased to 3 wt.% and the elemental composition of Ti reached ~0.15 at. % (with respect to the membrane profile), the cross-sectional EDX images indicated that the inorganic TiO_2 was still uniformly distributed in the PT membranes (see Figure S3). As discussed above, this could be attributed to the covalent bonds that formed between PLA and TiO_2, which enhanced the compatibility of organic-inorganic composites in the organic matrix due to the strong hydrophobic-hydrophobic interactions between PLA and PSF.

Mechanical properties of the prepared membranes were listed in Table S1. The results indicated that the tensile strength of the PP-0.5 was much lower compared with the P0 membrane. This could tentatively be attributed to the macroviods formed in the membrane sub-layer (as SEM shows). On the contrary, PT-0.5 exhibited enhanced tensile strength and it further increased with the increase of PLA/TiO_2 loadings. This finding is also in line with the revolution of the membrane structure, suggesting the finger-like and non-void sub-layer leads to improved mechanical properties (Yang *et al.* 2007). Thus, we propose that this prepared organic-inorganic nanocomposite can avert the disadvantages of organic macromolecular and inorganic nanoparticles in the modification of membrane structure, and hope this strategy can boost the development of new additives for membrane preparation.

Membrane surface physicochemical properties

The surface functional groups of the prepared PT membranes were investigated by using Raman spectra, and the results are shown in Figure 3(a). Comparing the PT membranes to the P0 membrane, the peaks at 143 cm^{-1} (belonging to TiO_2) emerged and intensified with the loading of PLA-TiO_2, demonstrating that PLA-TiO_2 was successfully blended into the PSF matrix. Furthermore, Figure 3(b) shows the water contact angle (WCA) of the prepared membranes. For PP-0.5, its WAC was slightly decreased to ~78.5° by adding 0.5 wt% PLA when compared with the P0 membrane. In stark contrast, the WCA of the PT-0.5 decreased to ~63.8° by adding merely 0.5 wt% PLA-TiO_2, and further decreased to ~56.3° with 3 wt% loading (PT-3), signifying the important role of inorganic TiO_2 for membrane surface hydrophilicity. Similarly with Figure 1(d), Figure 3(c) demonstrates that blending of PLA-TiO_2 endowed the PT membranes' distinct photoresponse ability under the UV band (i.e. 250–350 cm^{-1}) when compared with P0 and the PP-0.5, implying a photocatalytic potential of PT membranes with UV assistance.

On the other hand, the stability of PLA-TiO_2 in the membrane matrix was checked by conducting a 7-day continuous filtration and a 4-hour ultrasonic treatment, respectively. The results were also compared with the PPT-1 membrane, in which the membrane was prepared by blending PLA and TiO_2 to the PSF solution separately. Given that the PT-1 and the PPT-1 membrane possess the same components (i.e. PSF, PLA and TiO_2), the evolution of the TiO_2 during different treatment processes could be utilized to indicate the effect of inorganic-organic covalent bonds (i.e. bidentate chelating between PLA and TiO_2) on the anchorage of inorganic particles in the organic matrix.

Figure 3(d) shows the Raman spectra of the PT-1 and PPT-1 membrane before and after filtration (noted as @H) and ultrasonic treatment (noted as @U), respectively. In terms of PPT-1, it is clearly shown that the peak at 143 cm^{-1} representing TiO_2 becomes unnoticeable after post-treatments, indicating the weak compatibility of inorganic particles in the organic polymer. While, for PT-1, the peak related to TiO_2 was still obvious even after vigorous ultrasonic oscillation, signifying the enhanced anchoring strength of the PLA-TiO_2 in the polymer substance. Such observation could also be verified by the WCA measurements. As Figure 3(e) shows, the WCA of the PPT-1 increased by almost 20 degrees after 4 hours' ultrasonic treatment, which could be attributed to serious leakage of hydrophilic TiO_2 from the PSF matrix as in the Raman spectra noted above. This could also be proved by the WCA evolution of the T-1 membrane: a sharply decreased WCA was observed during both processes, suggesting the undesirable stability and anchorage of TiO_2 in PSF substance. As expected, PT-1 exhibited stable WCA during both processes, demonstrating the enhanced functionality and stability of inorganic-organic nanocomposites for decorating PSF membrane. We proposed such improvement should mainly be attributed to the presence of macromolecules; that is, PLA in nanocomposites, in which the PLA molecules combine with PSF molecules due to the hydrophobic-hydrophobic interactions or molecular entanglement. Given the covalent

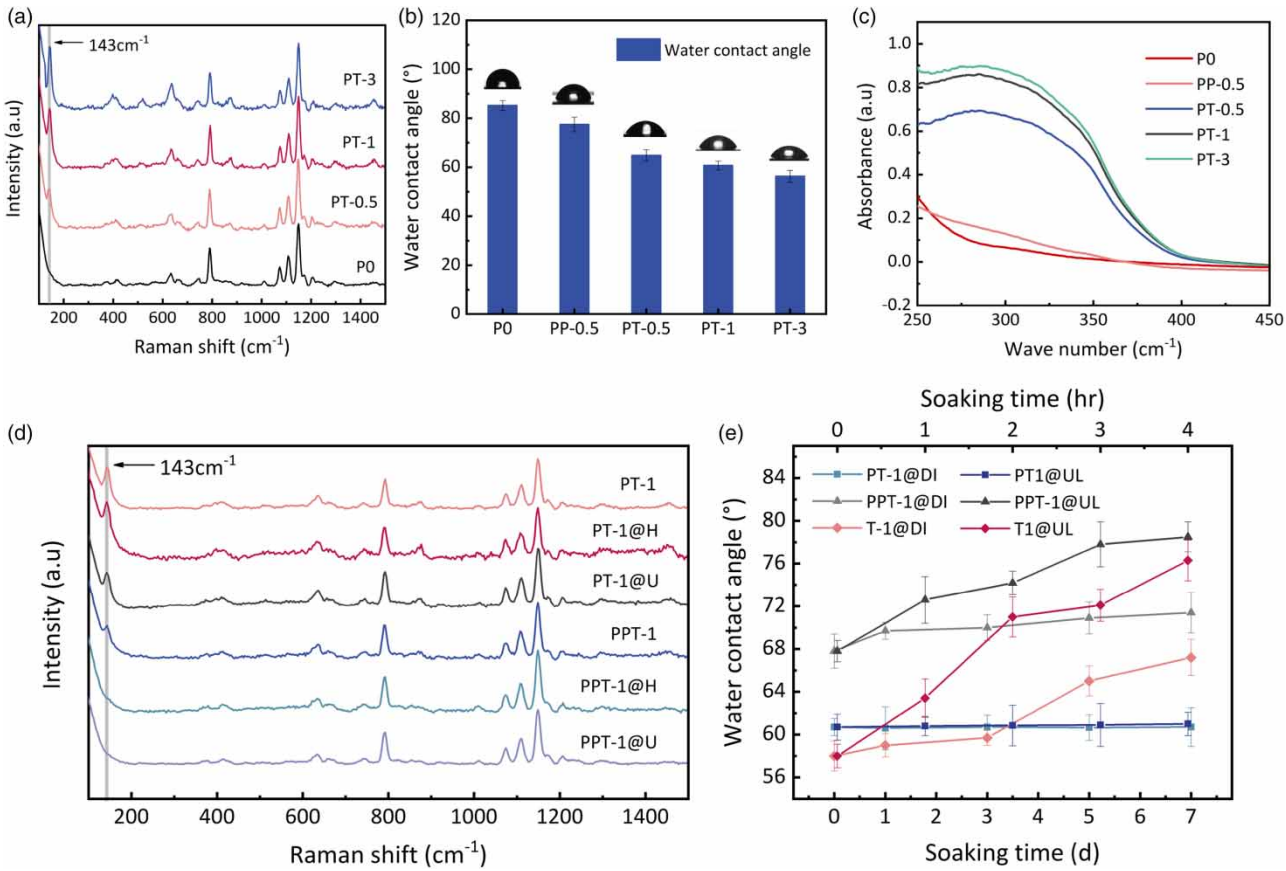

Figure 3 | (a) Raman spectra of P0 and PT membranes; (b) water contact angles and (c) UV–Vis spectra of the P0, PP and PT membranes; (d) Raman spectra of PT-1 and PPT-1 membrane and (e) water contact angle evolution of PT-1, PPT-1 and T-1 membranes undergoes 7 days' DI water filtration and 4 hours' ultrasound treatment.

bonds between PLA and TiO_2, the PLA finally act as bridges to bond the TiO_2 with the PSF matrix.

Permeability and separation properties

The permeability and selectivity of PT membranes were characterized by DI water flux and BSA sieving experiments, respectively. The filtration performance of the PT membranes as a function of PLA-TiO_2 loadings are illustrated in Figure 4. Moreover, to indicate the feasibility of PLA-TiO_2 in PSF UF membrane modifications, the results were also compared to PSF membranes that were prepared by other pore-forming additives.

As the figure shows, PT-0.5 achieved the best BSA filtration ability of 97% but a limited water permeability of 102.86 L/m^2 h/bar. This result was in line with the membrane surface morphology, in which the small surface pore diameter endowed the membrane with enhanced selectivity but the permeability was inhibited by the relatively low surface porosity. When the PLA-TiO_2 loading increased to 1 and 3%, the permeability of PT-1 and PT-3 increased dramatically to 229.7 and 280.3 L/m^2 h/bar, respectively, signifying the strong pore-forming ability of PLA-TiO_2 as the SEM images illustrated. In this situation, while the

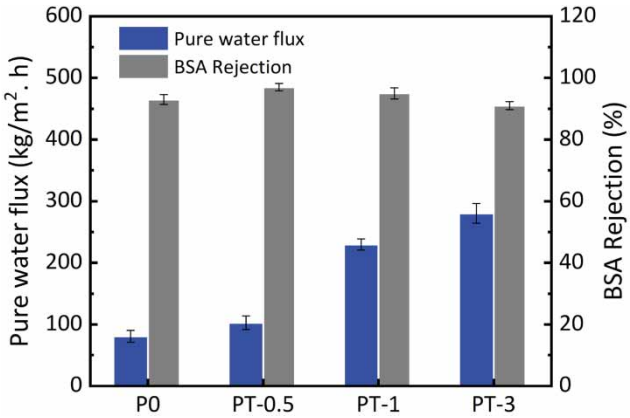

Figure 4 | Pure water flux and BSA rejection of the neat PSF membrane and PT membranes.

selectivity of the membranes suffers a slight decrease, the BSA rejection rate of the PT-1 and PT-3 can be maintained as high as 95 and 91%, respectively. As shown in Table S2, compared with the membranes that are prepared by using other conventional additives (e.g. PVP and LiCl), the PT-1 membrane exhibited enhanced filtration performance in both permeability and selectivity. Moreover, this improved filtration performance was obtained by adding merely 1% of PLA-TiO_2 to the casting solution, suggesting its strong ability for pore structure manipulations. Thus, we propose that the PT-1 membrane possesses a promising filtration performance for water purification purposes, particularly for the high demand of water-treatment processes on membrane permeability and selectivity. Therefore, the PT-1 membrane was selected to perform the following fouling experiment. On the other hand, the T-1 membrane was not involved into the antifouling experiments due to the inevitable leakage of TiO_2 in the membrane matrix during the filtration processes. Also, its dense top surface could not meet the high demands of the UF membrane for permeability.

Anti-fouling and self-cleaning performance of the prepared PT membranes

The antifouling performance of prepared membranes was challenged by filtering BSA solutions. Figure 5(a) compares the three cycles's filtration curves of PT-1 to that of the P0 membrane, in which simple physical cleaning was conducted after each 60 min filtration run.

In the first filtration cycle, both membranes underwent instant flux decline due to the occurrence of foulant adsorption and concentration polarization. Then, all membranes reached a steady state at the end of the fouling stage. Evidently, P0 suffered a serious flux reduction and its flux was only recovered to 60.1% of the initial value after physical cleaning (see Table 3). In contrast, PT-1 exhibited a temperate flux decline in the fouling stage and the flux recovered to 81.8% by performing physical rinsing, signifying an enhanced antifouling performance. Additionally, the long-term filtration also demonstrated the improved antifouling ability of PT-1. At the end of the 3rd cycle, PT-1 gained a recovered flux of 74.8% of its initial value, which

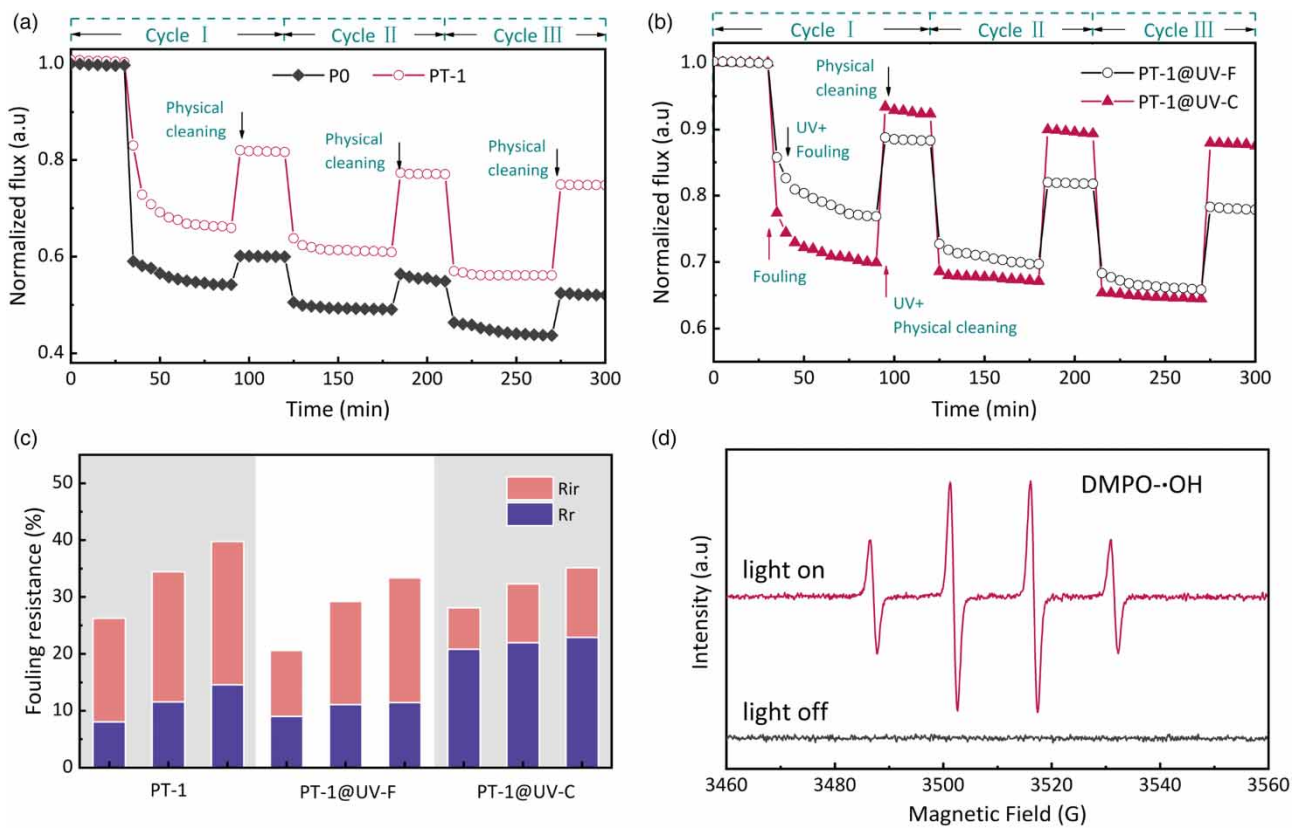

Figure 5 | (a) Fouling curves of P0 and PT-1 and (b) PT-1 membrane fouling curves for alternative pure water and BSA filtration (UV irradiation during physical cleaning process (@UV-C) or filtration process (@UV-F)); (c) fouling resistance parameters (R_t, R_r, R_{ir}) of prepared membranes; (d) DMPO spin-trapping ESR spectra of PT-1 membranes.

Table 3 | Flux recovery ratio (FRR) and specific fouling resistance (R_t, R_r and R_{ir}) in 3-cycle fouling experiments

	1st				2nd				3th			
Membrane	**FRR (%)**	**R_t (%)**	**R_r (%)**	**R_{ir} (%)**	**FRR (%)**	**R_t (%)**	**R_r (%)**	**R_{ir} (%)**	**FRR (%)**	**R_t (%)**	**R_r (%)**	**R_{ir} (%)**
P0	60.05	44.23	4.28	39.95	55.52	50.56	6.08	44.48	52.18	55.31	7.49	47.82
PT-1	81.77	26.26	8.04	18.23	77.13	34.42	11.55	22.88	74.83	39.74	14.58	25.17
PT-1@UV-F	88.42	20.59	9.01	11.58	81.86	29.22	11.09	18.14	78.05	32.09	11.43	21.95
PT-1@UV-C	92.72	28.10	20.82	7.28	89.63	32.33	21.96	10.37	87.25	36.15	22.91	12.25

was much better than that of P0 (52.2%). This observation can tentatively be attributed to the distinct inorganic-organic conformation of the PLA-TiO_2, in which the hydrophilic TiO_2 gifts the membrane enhanced surface hydrophilicity and the PLA segments made the nanocomposite firmly anchored to the polymer substance, eventually endowing the PT membranes with enhanced and stable antifouling performance in long-term filtration runs.

On the other hand, thorough membrane cleaning is now highly reliant on chemical cleaning and chemical detergent (e.g. HCl, NaOH and NaClO) in practical water treatment processes (Yu *et al.* 2020). However, the usage of chemical detergent not only generates environmental pollution and water safety issues due to the improper discharge or formation of disinfection by-products, but also has an adverse impact on the physicochemical properties and performance of the organic membranes (Zhang *et al.* 2017). Given that the prepared PT membranes possess responsiveness under UV irradiation, two strategies were designed to explore the feasibility of UV irradiation for membrane fouling mitigation. For the first, the membrane was exposed to UV light during the 60 min filtration process (named UV-F), but in the second strategy, UV irradiation was only employed during the 5 min physical cleaning stage (named UV-C). The effects of the above strategies on membrane fouling propensities were evaluated by performing a three cycle filtration, and the fouling curves are shown in Figure 5(b).

In the first cycle, the filtration conducted with UV irradiation (PT-1@UV-F) alleviated the membrane flux drop, and an improved recovered flux of 88.4% was obtained after physical cleaning. However, the recovered flux of PT-1 decreased gradually as the filtration went on, and the membrane flux recovered to 78.1% at the end of the 3rd cycle, which is similar to that fouled without UV assistance. As a contrast, in the first filtration cycle, PT-1 achieved a promising recovered flux of 92.7% when incorporating the UV irradiation with physical cleaning (PT-1@UV-C). More importantly, the recovered flux of PT-1 can be maintained at ~88% at the end of the 2nd and 3rd cycle, signifying the feasibility of UV-assisted physical cleaning in the fouling mitigation of the PT-1 membrane. To confirm the effect of photocatalytic oxidation on the fouling of the PT membrane with UV responsiveness, the fouling curves of the PP membranes were measured under different UV irradiation conditions. In Figure S4, both membranes underwent similar fouling propensity, and the fouling curves were not changed by UV irradiation. This observation is in stark contrast with Figure 5(b), suggesting the distinct fouling behavior of the PT membrane between the UV-F and UV-C processes could be attributed to its UV responsiveness and the photocatalytic oxidation effect.

For detail, the specific fouling resistances calculated from different strategies are shown in Figure 5(c), and their values are listed in Table 3. It clearly shows that in the normal fouling procedure, while the total fouling resistance (R_t) of PT-1 increased with filtration cycles, the irreversible fouling (R_{ir}) and reversible fouling (R_r) contributed almost equally to membrane fouling resistance. However, the R_t and its specific compositions were significantly changed under UV irradiation. In terms of the UV-F strategy, both the R_t and R_{ir} of PT-1 decreased in the 1st cycle, but the ratio of R_{ir} to R_t increased dramatically when the filtration cycles progressed. At the end of the 3rd cycle, nearly ~75% of the R_t was assigned to the R_{ir}, indicating long-term UV irradiation aggravated membrane irreversible fouling. In stark contrast, the UV-C strategy exhibited a distinct ability to alleviate fouling resistance, especially for the R_{ir}, and the increase of R_{ir} was maintained at a very low rate in the whole filtration experiment.

In order to interpret the mechanism of UV irradiation on the fouling behaviors of the PT-1 membrane, electron spin resonance (ESR) was used to investigate the generation of active radical species on the PT-1 membrane surface. In Figure 5(d), strong DMPO-·OH signals were detected when UV light illuminated the PT-1 membrane immersed in water, demonstrating the generation of ·OH in UV-F

and UV-C processes. Given the strong oxidizing ability of ·OH for organic macromolecules (e.g. BSA), it was believed that the distinct fouling behaviors could relate to the synergistic effect between photocatalytic oxidation and membrane sieving.

Figure 6 illustrates the fouling and antifouling mechanisms that are related to UV-F and UV-C strategies, respectively. Given that the max mass transfer distance of ·OH in water was no more than 90 nm (Chen *et al.* 2019), the TiO_2 embedded in the superficial portion of the PT membrane may play a vital role in the photocatalytic oxidation of BSA. In terms of the UV-F strategy, the membrane hydrophilicity was further improved via the reaction between TiO_2 and water molecules (Méricq *et al.* 2015), and the generated oxidative ·OH and reactive oxygen species (e.g. $\cdot O_2^-$, $HO_2\cdot$) may inhibit the BSA molecules to bond with the membrane surface (Yang *et al.* 2005), thus resulting in a released flux decline. However, in the UV-assisted filtration process, the BSA molecules could also be decomposed into small segments due to the presence of oxidative ·OH (Damodar *et al.* 2009), and the small segments can easily enter into pores with the convection current and result in irreversible fouling. We propose that is why the R_{ir} increased with ongoing filtration in the UV-F process. On the other hand, the UV-C strategy exhibited a strong ability to reduce the irreversible membrane fouling. In the UV-assisted rinsing process, the active radicals generated by TiO_2 facilitated the desorption of BSA from the membrane surface and pores, and the desorpted BSA could be easily rinsed off by vigorous laminar flow (crossflow), thus resulting in enhanced cleaning efficiency. Also, in the absence of convection flow (i.e. TMP = 0 MPa), the effect of BSA decomposition on membrane irreversible fouling could be neglected. As a consequence, for the prepared PT membrane, the UV-assisted physical cleaning strategy was a better choice with the consideration of both fouling mitigation and energy consumption.

Moreover, the membranes' thermal properties before and after 24 hours' UV irradiation were investigated by performing thermogravimetric (TG) analysis. In Figure 7, PT-1 shows the first weight loss at the temperature of 300–400 °C, which corresponds to the TG curves of PLA-TiO_2, confirming that PLA-TiO_2 had interacted and were homogeneously blended with the polymer matrix. The second weight loss observed around 500–600 °C accounts for the decomposition of the PSF polymer. Clearly, after 24 hours' exposure to UV light, the TG curves of the PT membrane almost stay the same, indicating the limited impact of UV

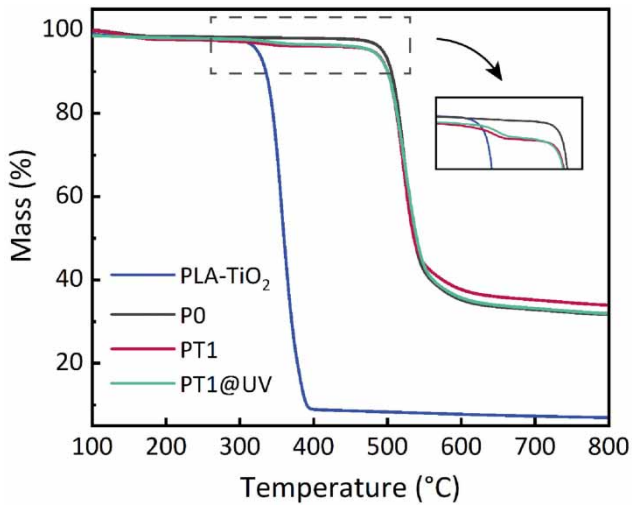

Figure 7 | TG curves of PLA-TiO_2 nanocomposite, P0 membrane and PT1 membranes before and after UV irradiation (PT1@UV).

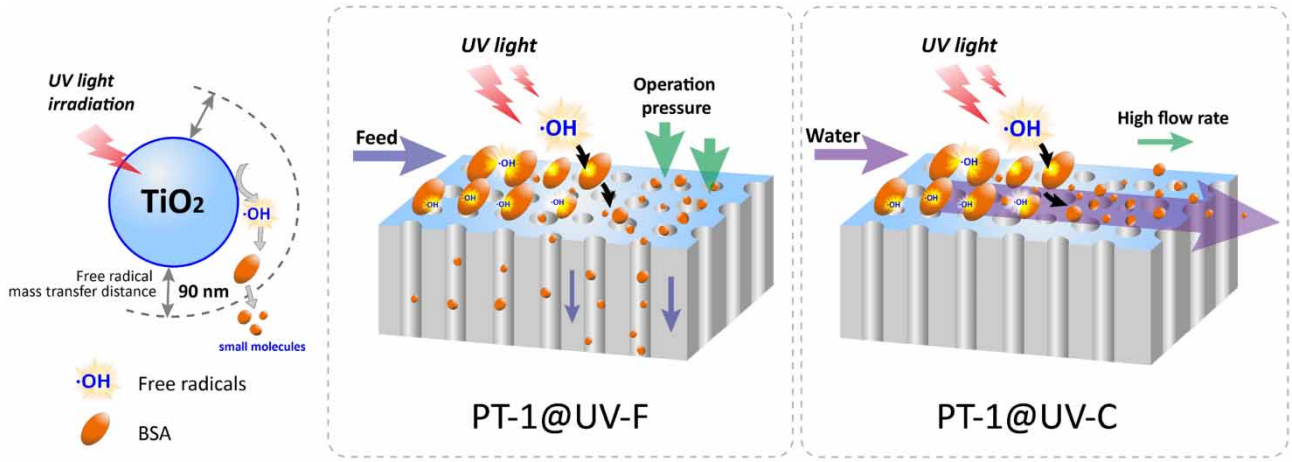

Figure 6 | Schematic illustration of photocatalytic processes in different strategies.

exposure on the membrane integrity and thermal properties. Also, given that only 5 minutes' UV exposure was needed after each filtration cycle, there are reasons to propose that the UV-C strategy was a valid, cost-effective and sustainable way to mitigate fouling of the PT membrane.

CONCLUSIONS

In this study, an organic-inorganic nanocomposite, PLA-TiO_2, has been intentionally synthesized as both pore forming additives and antifouling modifiers, and then employed for PSF membrane preparation. The morphology of the PT membranes demonstrated that the addition of PLA-TiO_2 gifts the membrane with porous surfaces and narrowed pore size distributions when compared with adding PLA only. Also, the PLA-TiO_2 exhibited improved compatibility and stability in PSF substance compared with TiO_2, which endowed the membrane with distinct responsiveness under UV irradiation. Moreover, the antifouling performance of the PT membrane was further enhanced with a UV-assisted physical cleaning process (UV-C), in which both the reversible and irreversible fouling were reduced significantly, signifying the synergistic effect between photocatalytic oxidation and hydraulics in membrane fouling mitigations. We anticipate numerous organic-inorganic nanocomposites could be developed and applied for membrane preparation and functionalization in future, improving the sustainability of membrane technology in the water treatment process.

ACKNOWLEDGEMENTS

This study was jointly supported by the National Natural Science Foundation for Young Scientists of China (51808388), State Key Program of National Natural Science Foundation of China (51638011) and the Natural Science Foundation of Tianjin, China (No. 18JCQNJC76700). Y. Zhang gratefully acknowledges the support of Young Elite Scientists Sponsorship Program by China Association for Science and Technology (CAST).

DATA AVAILABILITY STATEMENT

All relevant data are included in the paper or its Supplementary Information.

REFERENCES

Chen, Y., Zhang, G., Liu, H. & Qu, J. 2019 Confining free radicals in close vicinity to contaminants enables ultrafast Fenton-like processes in the interspacing of MoS_2 membranes. *Angewandte Chemie International Edition* **58** (24), 8134–8138.

Damodar, R. A., You, S. J. & Chou, H. H. 2009 Study the self cleaning, antibacterial and photocatalytic properties of TiO_2 entrapped PVDF membranes. *Journal of Hazardous Materials* **172** (2–3), 1321–1328.

Feng, S., Zhang, F., Ahmed, S. & Liu, Y. 2019 Physico-mechanical and antibacterial properties of PLA/TiO_2 composite materials synthesized via electrospinning and solution casting processes. *Coatings* **9** (8), 525.

Green, I. X., Tang, W., Neurock, M. & Yates, J. T. 2012 Localized partial oxidation of acetic acid at the dual perimeter sites of the Au/TiO_2 catalyst – formation of gold ketenylidene. *Journal of the American Chemical Society* **134** (33), 13569–13572.

Han, M.-J. & Nam, S.-T. 2002 Thermodynamic and rheological variation in polysulfone solution by PVP and its effect in the preparation of phase inversion membrane. *Journal of Membrane Science* **202** (1), 55–61.

Jafarpour, M., Ghahramaninezhad, M. & Rezaeifard, A. 2014 Synthesis, characterization and catalytic activity of oleic acid-coated TiO_2 nanoparticles carrying MoO_2 (acac)2 in the oxidation of olefins and sulfides using economical peroxides. *New Journal of Chemistry* **38** (7), 2917–2926.

Jhaveri, J. H. & Murthy, Z. V. P. 2016 A comprehensive review on anti-fouling nanocomposite membranes for pressure driven membrane separation processes. *Desalination* **379**, 137–154.

Khan, A., Sherazi, T. A., Khan, Y., Li, S., Naqvi, S. A. R. & Cui, Z. 2018 Fabrication and characterization of polysulfone/modified nanocarbon black composite antifouling ultrafiltration membranes. *Journal of Membrane Science* **554**, 71–82.

Lee, S. J., Han, S. W., Yoon, M. & Kim, K. 2000 Adsorption characteristics of 4-dimethylaminobenzoic acid on silver and titania: diffuse reflectance infrared Fourier transform spectroscopy study. *Vibrational Spectroscopy* **24** (2), 265–275.

Li, S., Cui, Z., Zhang, L., He, B. & Li, J. 2016 The effect of sulfonated polysulfone on the compatibility and structure of polyethersulfone-based blend membranes. *Journal of Membrane Science* **513**, 1–11.

Li, J., Liu, F., Qin, Y., He, J., Xiong, Z., Deng, G. & Li, Q. 2017 A novel natural hirudin facilitated anti-clotting polylactide membrane via hydrogen bonding interaction. *Journal of Membrane Science* **523**, 505–514.

Liu, Y., Koops, G. H. & Strathmann, H. 2003 Characterization of morphology controlled polyethersulfone hollow fiber membranes by the addition of polyethylene glycol to the dope and bore liquid solution. *Journal of Membrane Science* **223** (1–2), 187–199.

Liu, J., Han, L., An, N., Xing, L., Ma, H., Cheng, L., Yang, J. & Zhang, Q. 2017 Enhanced visible-light photocatalytic activity of carbonate-doped anatase TiO_2 based on the electron-withdrawing bidentate carboxylate linkage. *Applied Catalysis B: Environmental* **202**, 642–652.

Loh, C. H. & Wang, R. 2013 Insight into the role of amphiphilic pluronic block copolymer as pore-forming additive in PVDF membrane formation. *Journal of Membrane Science* **446** (11), 492–503.

Luo, X., Liang, H., Qu, F., Ding, A., Cheng, X., Tang, C. Y. & Li, G. 2018 Free-standing hierarchical α-MnO_2@CuO membrane for catalytic filtration degradation of organic pollutants. *Chemosphere* **200**, 237–247.

Méricq, J. P., Mendret, J., Brosillon, S. & Faur, C. 2015 High performance PVDF-TiO_2 membranes for water treatment. *Chemical Engineering Science* **123**, 283–291.

Qu, Q., Geng, H., Peng, R., Cui, Q., Gu, X., Li, F. & Wang, M. 2010 Chemically binding carboxylic acids onto TiO_2 nanoparticles with adjustable coverage by solvothermal strategy. *Langmuir* **26** (12), 9539–9546.

Rabiee, H., Farahani, M. H. D. A. & Vatanpour, V. 2014 Preparation and characterization of emulsion poly(vinyl chloride) (EPVC)/TiO_2 nanocomposite ultrafiltration membrane. *Journal of Membrane Science* **472**, 185–193.

Shi, Y., Huang, J., Zeng, G., Cheng, W. & Hu, J. 2019 Photocatalytic membrane in water purification: is it stepping closer to be driven by visible light? *Journal of Membrane Science* **584**, 364–392.

Wang, L. K., Chen, J. P., Hung, Y. T. & Shammas, N. K. 2011 *Membrane and Desalination Technologies*. Chapter 12, pp. 525–558. Humana Press.

Xing, J., Liang, H., Cheng, X., Yang, H., Xu, D., Gan, Z., Luo, X., Zhu, X. & Li, G. 2019 Combined effects of coagulation and adsorption on ultrafiltration membrane fouling control and subsequent disinfection in drinking water treatment. *Environmental Science and Pollution Research* **26** (33), 33770–33780.

Xiong, Z., Lin, H., Zhong, Y., Qin, Y., Li, T. & Liu, F. 2017 Robust superhydrophilic polylactide (PLA) membranes with a TiO_2 nano-particle inlaid surface for oil/water separation. *Journal of Materials Chemistry A* **5** (14), 6538–6545.

Xu, Z., Wu, T., Shi, J., Teng, K., Wang, W., Ma, M., Li, J., Qian, X., Li, C. & Fan, J. 2016 Photocatalytic antifouling PVDF ultrafiltration membranes based on synergy of graphene oxide and TiO_2 for water treatment. *Journal of Membrane Science* **520**, 281–293.

Yang, G. Q., Zhao-Hui, L. I., Lin, Z. X., Wang, X. X. & Liu, P. 2005 Investigation of TiO_2 photocatalytic degradation of bovine serum albumin. *Spectroscopy & Spectral Analysis* **25** (8), 1309–1311.

Yang, Y., Zhang, H., Wang, P., Zheng, Q. & Li, J. 2007 The influence of nano-sized TiO_2 fillers on the morphologies and properties of PSF UF membrane. *Journal of Membrane Science* **288** (1–2), 231–238.

You, S. J., Semblante, G. U., Lu, S. C., Damodar, R. A. & Wei, T. C. 2012 Evaluation of the antifouling and photocatalytic properties of poly(vinylidene fluoride) plasma-grafted poly(acrylic acid) membrane with self-assembled TiO_2. *Journal of Hazardous Materials* **237–238**, 10–19.

Yu, H., Li, X., Chang, H., Zhou, Z., Zhang, T., Yang, Y., Li, G., Ji, H., Cai, C. & Liang, H. 2020 Performance of hollow fiber ultrafiltration membrane in a full-scale drinking water treatment plant in China: a systematic evaluation during 7-year operation. *Journal of Membrane Science* **613**, 118469.

Zhang, Y., Wang, J., Gao, F., Chen, Y. & Zhang, H. 2017 A comparison study: the different impacts of sodium hypochlorite on PVDF and PSF ultrafiltration (UF) membranes. *Water Research* **109**, 227–236.

Zhao, S., Wang, Z., Wei, X., Zhao, B., Wang, J., Yang, S. & Wang, S. 2011 Performance improvement of polysulfone ultrafiltration membrane using PANiEB as both pore forming agent and hydrophilic modifier. *Journal of Membrane Science* **385–386**, 251–262.

Zhou, Z., Liu, L. & Yuan, W. 2019 A superhydrophobic poly(lactic acid) electrospun nanofibrous membrane surface-functionalized with TiO_2 nanoparticles and methyltrichlorosilane for oil/water separation and dye adsorption. *New Journal of Chemistry* **43** (39), 15823–15831.

First received 27 August 2020; accepted in revised form 13 November 2020. Available online 27 November 2020